1   Electronic Supplementary Information

2

3   Designing a solar interfacial evaporator based on tree

4   structures for great coordination of water transport

5   and salt rejection

6   Zhicheng Xu[a], Xueqin Ran[a], Zhijie Zhang[a*] Mingfeng Zhong[a], Da Wang[b], Pengping

7   Li[c], Zhihong Fan[c]

8

9   a. School of Materials Science and Engineering, South China University of Technology,

10   Guangzhou 510640, China

11   b. School of Physics and Optoelectronics, South China University of Technology, Guangzhou

12   510640, China

13   c. Key Laboratory of Harbor and Marine Structure Durability Technology Ministry of

14   Communications, Guangzhou 510230, China

15   *Corresponding author. E-mail address: imzhang@scut.edu.cn (Zhijie Zhang)

16

17   **This PDF file includes:**

18   S1. Materials and Methods

19   S2. Numerical Simulation

20   S3. Supplementary Figures and Tables

21   S4. References

22

S1 Materials and Methods

S1.1 Materials

Kaolin powder was provided by Guangdong Changlong Ceramics Co. LTD, and it was dried at 120 ℃ for 12 hours and sifted through 200 mesh before use. Calcium phosphate was purchased from Tianjin Kemiou Chemical Reagent Co. Ltd. Sodium hexametaphosphate was purchased from Tianjin Fuchen Chemical Reagent Co. LTD. Food grade bacterial cellulose hydrogel was purchased from Jinan Jinhuafang Food Technology Co. LTD and was broken in a blender before use. The multilayer graphene oxide (MGO) was provided by Soochow Hengqiu Graphene Technology Co. Ltd. Sodium dodecyl sulfate and polyacrylamide were supplied by Shanghai Macklin Biochemical Co. Ltd. NaCl was obtained from Sinopharm Chemical Reagent Co. Ltd.

S1.2 Preparation of porous ceramic and MGO dispersion

The ceramic particles consist of kaolin, calcium phosphate and sodium hexametaphosphate in a mass percentage of 93:6:1. In order to obtain a stable and highly dispersed slurry, we used bacterial cellulose (BC) hydrogel with a water content of 99.64 % as the dispersion medium. The ceramic aggregate and bacterial cellulose are mixed evenly in a teflon mill pot and ball-milled for 3.5 hours at 350 rpm. The ceramic aggregate content was adjusted between 15 wt% and 30 wt%. For comparison, BC and pure water were used as dispersion mediums (the slurries obtained were marked as BC, H_2O) to demonstrate the stability of the slurry, their solid contents were set as 15 wt%. The uniform slurry was then poured into a homemade mold for freeze-drying (Fig S1a, -45 ℃ is provided by the cold trap of the Freeze dryer to prepare short ceramic, and -78 ℃ is provided by dry ice-frozen ethanol solution to prepare long ceramic) on Freeze dryer (FD-1A-50) for 4 days. The dry ceramic billet was then kept at 500 ℃ for 1 hour to remove the organic matter, and then sintered at 1250 ℃ for 90 minutes to obtain the required porous ceramics. Before all the tests, we have cut off 3 mm of the bottom of the sintered ceramic along the Gradient direction.

For MGO dispersion, 0.02 g MGO and 0.004 g sodium dodecyl sulfate were added to 2 ml deionized water for ultrasonic treatment for 15 minutes. Finally, the disperse

solution is evenly applied to the surface of the ceramic with a brush and then dried naturally.

S1.3 Water absorption.

Cut off 3 mm of the bottom of the sintered ceramic along the Gradient direction, and then cut 6.5 cm upward to get the sample for capillary water absorption test, the sample were marked as (Solid content)-Direction like 15 wt%-Gradient. As shown in Fig S1b, the ceramic was hung on an iron wire to a hook at the bottom of the electronic balance plate and the water in the petri dish was lifted by a lifting platform, which submerge the bottom of the ceramic by 3 mm. The electronic balance was connected to a computer to record the changes in the quality data.

S1.4 Evaporation test.

As shown in Fig S1c, the porous ceramic was clamped by a foam so that it can float on the water. The simulated solar light was provided by xenon lamp (CHF-XM500, the wavelength spectrum ranges from 200 to 1100 nm.) equipped with an AM1.5 filter. The mass change was recorded by a weighing balance and the temperature was recorded by infrared thermal imager (FLIR E4). The solar evaporation experiments were carried out under the environment of 25 ± 2 °C and 50 ± 5 % relative humidity. The same procedure was carried out at the same environment without the solar steam generator or in dark conditions.

S1.5 Measurement of open porosity

The mean open porosity of porous ceramic was measured by gravimetric test method and the porosity can be calculated by the following formula:

$$\varepsilon = \frac{m}{\rho A L} \tag{S1}$$

where ε is the porosity, m is the mass of water soaked by porous ceramic (measured by a weighing balance (PTX-FA210S), ρ is the density of water, L is the height of the porous ceramic and A is the cross-sectional area, which can be calculated by measuring the radius of the ceramics with vernier calipers.

S1.6 Characterization

The morphologies were observed by scanning electron microscopy (SEM, NOVA NANOSEM 430), Micro-CT (Quantum GX II) and high-resolution transmission electron microscope (JEM-2100F). The phase composition of the material was detected by XRD (X'Pert PRO MPD). The light absorption was measured by UV/VIS/NIR spectrometer (Lambda 750S, PerkinElmer, America). The metal ions concentration was measured by ICP-OES (Optima 8300).

S1.7 Calculation of evaporation rate and solar energy utilization efficiency

In our study, the evaporation rate was calculated in terms of the projected area (A), which is equal to the area of the circular cross section at the top of the ceramic. The solar energy utilization efficiency of the solar steam generator was calculated as the percentage of the energy that used for water evaporation compared to the energy irradiated to the evaporation surface. The general calculation formula is as follows:

$$\eta = \Delta \dot{m} H_{Lv}/P_{in} \tag{S2}$$

where η is the solar energy utilization efficiency, $\Delta \dot{m}$ is the net water mass-change rate given by $\Delta \dot{m} = \dot{m}_{w/evaporate\ under\ sun} - \dot{m}_{w/evaporate\ in\ dark}$ with a unit of kg m^{-2} h^{-1}, H_{Lv} is the enthalpy of liquid-vapor phase transition at the operation temperature (we used 2400 j g^{-1} in our calculations) and P_{in} is the intensity of simulated solar light irradiation. Because the test was carried out when the evaporation surface was heated to a stable temperature, the sensible heat was ignored.

S2 Numerical simulation

S2.1 Capillary suction

S2.1.1 Geometry and mesh generation

The geometries were created in the software DesignModeler and the software Mesh was used to carried out mesh generation. The sizes of the capillaries and the mesh are

105 shown in Fig. S2a. To solve the initial saturation mutation problem at inlet and reduce

106 the disturbance at the outlet, denser meshes were set near approaching the bottom and

107 the top of the models. Because the calculation is simple, a smaller mesh size was used

108 to ensure the accuracy of the calculation. As a result, the elements of the three models

109 are: 4686 for Gradient-OD, 3318 for Isodiametric and 4686 for Gradient.

110 S2.1.2 Mathematical model, volume of fluid (VOF) method and

111 boundary condition

112   We used commercial software Fluent 19.0 to understand the process of capillary

113 suction. Fluent is one of the most commonly used fluid dynamics simulation software.

114 It employs a simple and fast finite volume method to solve the governing equations and

115 produce the distribution field of relevant physical quantities. Capillary suction is a two-

116 phase flow problem. In a hydrophilic capillary, the wetting phase (water) will displace

117 the non-wetting phase (air). An interface exists between two immiscible fluids and we

118 can track it by solving the Navier-Stokes equation and momentum equation:

119 Continuity:

$$\frac{\partial \rho}{\partial t} + \frac{\partial (\rho u)}{\partial x} + \frac{\partial (\rho v)}{\partial y} = 0$$

120   (S3)

121 X-momentum:

$$\frac{\partial (\rho u)}{\partial t} + \frac{\partial (\rho u u)}{\partial x} + \frac{\partial (\rho u v)}{\partial y} = -\frac{\partial P}{\partial x} + \left[\frac{\partial}{\partial x}\left(\mu \frac{\partial u}{\partial x} \right) + \frac{\partial}{\partial y}\left(\mu \frac{\partial u}{\partial y} \right) \right] + S_x$$

122   (S4)

123 Y-momentum:

$$\frac{\partial (\rho v)}{\partial t} + \frac{\partial (\rho v u)}{\partial x} + \frac{\partial (\rho v v)}{\partial y} = -\frac{\partial P}{\partial y} + \left[\frac{\partial}{\partial x}\left(\mu \frac{\partial v}{\partial x} \right) + \frac{\partial}{\partial y}\left(\mu \frac{\partial v}{\partial y} \right) \right] + S_y$$

124   (S5)

125 here u and v are the fluid velocity component in x-direction and y-direction, ρ is the

126 fluid density, μ is the viscosity and P is the pressure. In the momentum equation, S_x

127 and S_y are the source terms that include the contribution of gravity and surface tension.

128   In 1981, Hirt et al used the volume of fluid (VOF) method to track an interface

129 firstly. They tracked the volume fraction of each phase instead of the interface itself,

130 and the interface was reconstructed from the values of volume fraction.[1, 2] In order to

131 track the interface between two immiscible fluids, the VOF method uses a color

132 function which have a value varying from 0 to 1 (0 and 1 represent the control volume

133 is entirely filled with one or the other of the phases).[3] A function $\chi(x,y,t)$ is defined to

134 represent the change in volume fraction. If $\chi(i,j) = 1$, the cell i,j is full of the wetting

135 phase, and if $\chi(i,j) = 0$, the cell i,j is full of the non-wetting phase. For function value

136 between 0 and 1, the cell contains interface. In a Eulerian calculation, an averaging of

137 the flow properties is required to compute the flow of fluid through the mesh, thus the

138 density and viscosity become:

139
$$\rho = \chi\rho_1 + (1 - \chi)\rho_2 \qquad (S6)$$

140
$$\mu = \chi\mu_1 + (1 - \chi)\mu_2 \qquad (S7)$$

141 Subscripts 1 and 2 represent the wetting and non-wetting phases, respectively.

142 Accordingly, the governing equations become:

143 Continuity:

144
$$\frac{\partial(\chi\rho_1)}{\partial t} + \nabla\chi\rho_1 u_1 = 0 \qquad (S8)$$

145
$$\frac{\partial[(1 - \chi)\rho_2]}{\partial t} + \nabla[(1 - \chi)\rho_2 u_2] = 0 \qquad (S9)$$

146 Momentum:

147
$$\frac{\partial(\chi\rho_1 u_1)}{\partial t} + \nabla[\chi\rho_1 u_1 u_1] = -\Delta P_1 + \nabla[\chi\mu_1(\nabla u_1 + \nabla u_1^T)] + \chi\rho_1 g + \vec{F} \qquad (S10)$$

148
$$\frac{\partial([(1 - \chi)\rho_2 u_2])}{\partial t} + \nabla[(1 - \chi)\rho_2 u_2 u_2] =$$

149
$$-\Delta P_2 + \nabla[(1 - \chi)\mu_2(\nabla u_2 + \nabla u_2^T)] + (1 - \chi)\rho_2 g + \vec{F} \qquad (S11)$$

150 here $\vec{F}$ is the source term including the contribution of surface tension, which can be

151 calculate by the Continuous surface force model (CSF) proposed by Brackbill.[4]

152   After the mesh profile was generated and imported into Fluent, the relevant

153 parameters were set and the boundary condition, material properties and solver

154 parameters ware defined as the following:

155 **Table S1** Key settings for the CFD model

Boundary conditions	
Inlet	Pressure inlet, 0 Pa. The initial volume fraction of the wetting phase is 1.
Outlet	Pressure outlet, 0 Pa.
No-flux boundaries	0 degree as the contact angle between the wicking liquid and boundaries.
Material properties	
Water density ρ_1	998.2 kg m^{-3}
Air density ρ_2	1.225 kg m^{-3}
Water dynamic viscosity μ_1	1.003e^{-3} kg m^{-1} s^{-1}
Air dynamic viscosity μ_2	1.7894e^{-5} kg m^{-1} s^{-1}
Solver parameters	
Method	SIMPLE
Analysis type	Transient
Time Step Size	1e^{-6} s
Max iterations per loop	30
Total Time steps	500

156 S2.2 Salt diffusion

157 S2.2.1 Geometry and mesh generation

158 The geometries are created in the software DesignModeler and the software Mesh
159 was used to carried out mesh generation. The sizes of the capillaries and the divided
160 mesh are shown in Fig. S2b. The elements of the model were 4279. Flip the model to
161 form Gradient-OD and Gradient, respectively.

162 S2.2.2 Mathematical model and boundary condition

163 In this section, a CFD model is formulated by the commercial software Fluent 19.0

164   too. In our simulation, the top meniscus is assumed to be a rigid interface because water

165   can always be supplied in time under the capillary pressure. Below the meniscus, the

166   capillary is filled with sodium chloride aqueous solution. With the evaporation of water

167   from the meniscus, the salt left behind leads to a concentration gradient and then the

168   salt diffuses down. This process mainly involves two hydrodynamic problems: liquid

169   evaporation and species diffusion. We solve the problem by writing UDF files and

170   using the Species Transport model of Fluent. In addition, Multiphase (Volume of Fluid)

171   was also used in this simulation because the water was supplied by surface tension (See

172   section 2.1 for the details). Finally, we considered the process as laminar flow and the

173   Energy equation was also used because evaporation involves energy transfer.

174   For the liquid phase, the continuity equation, momentum balance equation and the

175   general species transport equation are well known as:

176
$$\frac{\partial \rho \varepsilon_i}{\partial t} + \rho \varepsilon_i \nabla v_i = 0 \qquad \text{(S12)}$$

177
$$\frac{\partial \left(\rho \varepsilon_i \overrightarrow{v} \right)}{\partial t} = -\varepsilon_i \nabla p - \mu_l \nabla \cdot \left(\rho \varepsilon_i \overrightarrow{v_i} \overrightarrow{v_i} \right) + \nabla \cdot \tau \qquad \text{(S13)}$$

178
$$\frac{\partial}{\partial t}(\rho \varepsilon_i) = -\nabla \cdot \underset{J_i}{\overrightarrow{}} - \nabla \left(\rho \underset{v_i}{\overrightarrow{}} \varepsilon_i \right) + S_i \qquad \text{(S14)}$$

179   where:

180   ε_i=local mass fraction of species i,

181
$$\sum_{1}^{2} \varepsilon_i = 1 \qquad \text{(S15)}$$

182   ρ=the density of the solution;

183   v_i = velocity;

184   p = the pressure of the solution;

185   μ_l= the liquid dynamic viscosity;

186   τ= stress tensor;

187   J_i= the diffusion flux of species i, which arises due to the gradients of concentration

188 and was calculated bases on Fick' law:

$$J_i = -\rho D_i \nabla \varepsilon_i \qquad \text{(S16)}$$

190 D_i= diffusion coefficient, as for salt, it was set as 2.88e^{-5} m^2 s^{-1} for all capillary models

191 so that it won't take so much time to realize a marked concentration change;

192 S= source term due to water evaporation.

193   In our UDF file, by setting a saturation evaporation temperature T_{sat}, evaporation

194 will occur when the temperature T_1 of the solution is higher than T_{sat}. The calculation

195 formula of evaporation mass is as follows:

$$m = h_m \rho \varepsilon_w \left| \frac{T_1 - T_{sat}}{T_{sat}} \right| \qquad \text{(S17)}$$

197 where h_m is the evaporation coefficient and was set as 1.5, ε_w is the mass fraction of

198 water.

199   Then, the boundary conditions were set in Fluent. The inlet was set as pressure inlet

200 with 0 static pressure so that the solution was transported by surface tension without

201 any external pressure. The outlet was set as pressure outlet without any flow so that the

202 water is loss by evaporation only. As for two side walls, they were set as hydrophilic

203 wall with a contact angle of 70°. The capillaries were pre-wetted with the mixture

204 solution before the calculation and the initial mass fraction of salt was set as 5 %. For

205 evaporation, the T_{sat} was set as 285 K and the initial temperature of the solution was

206 set as 300 K.

207   Finally, the problem was solved by Fluent with a transient calculation model and

208 the Time Step size was set as 2e^{-7} s to ensure convergence and high accuracy. In our

209 calculation, the crystallization of salt wasn't considered because the transport time is

210 short enough that the concentration won't reach the crystallization concentration (26.52

211 %)

212

S3 Supplementary Figures and Tables
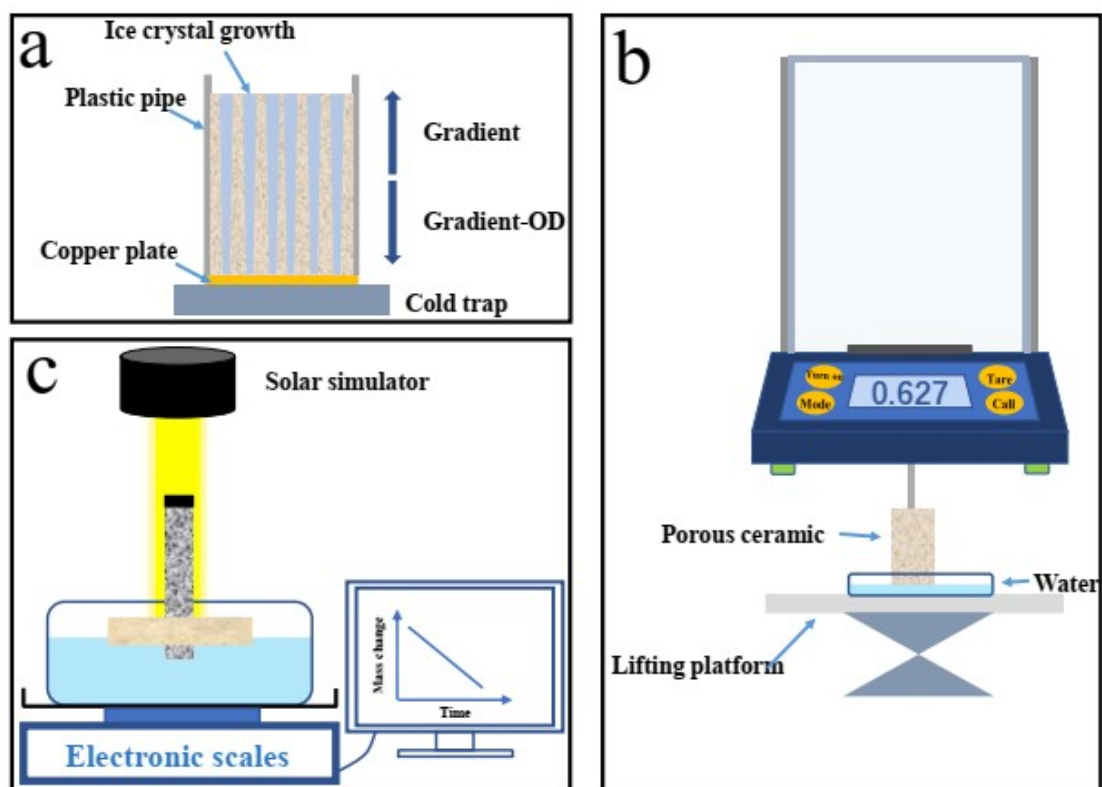
Fig. S1 Schematic diagram of: (a) Slurry freezing. (b) Water absorption. (c) Evaporation test.

218
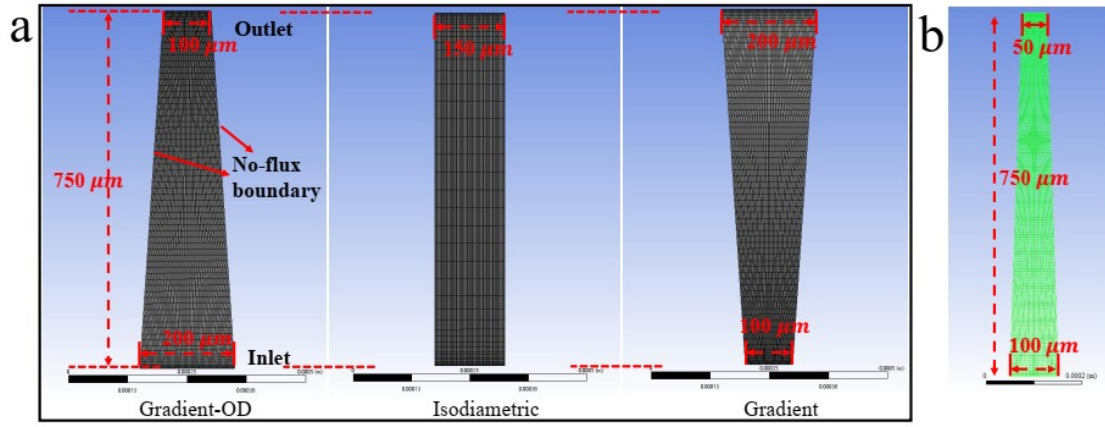
219 **Fig. S2** The geometries and meshes of: (a) Capillary suction. (b) Salt diffusion.

220
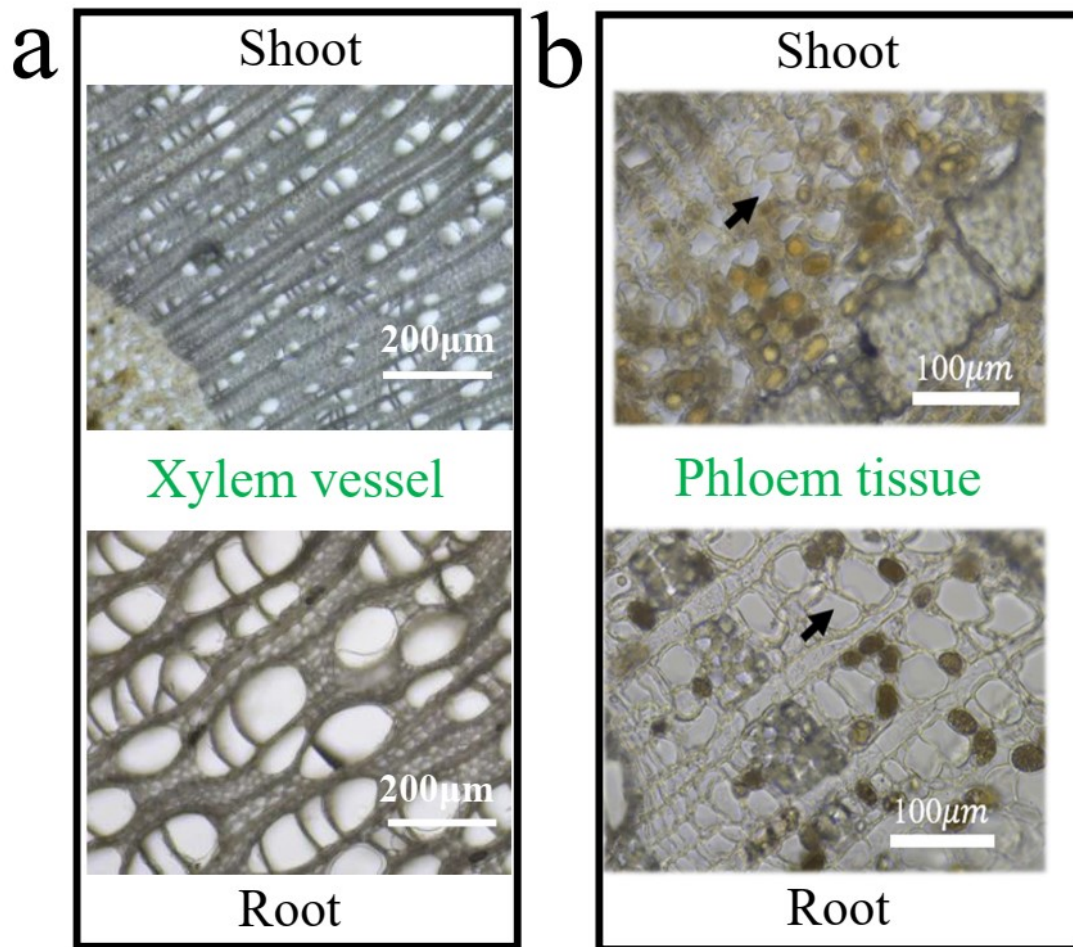
Fig. S3 (a) Xylem vessel and (b) Phloem tissue micrographs of current year growth from a wide diameter root and a narrow shoot of poplar trees
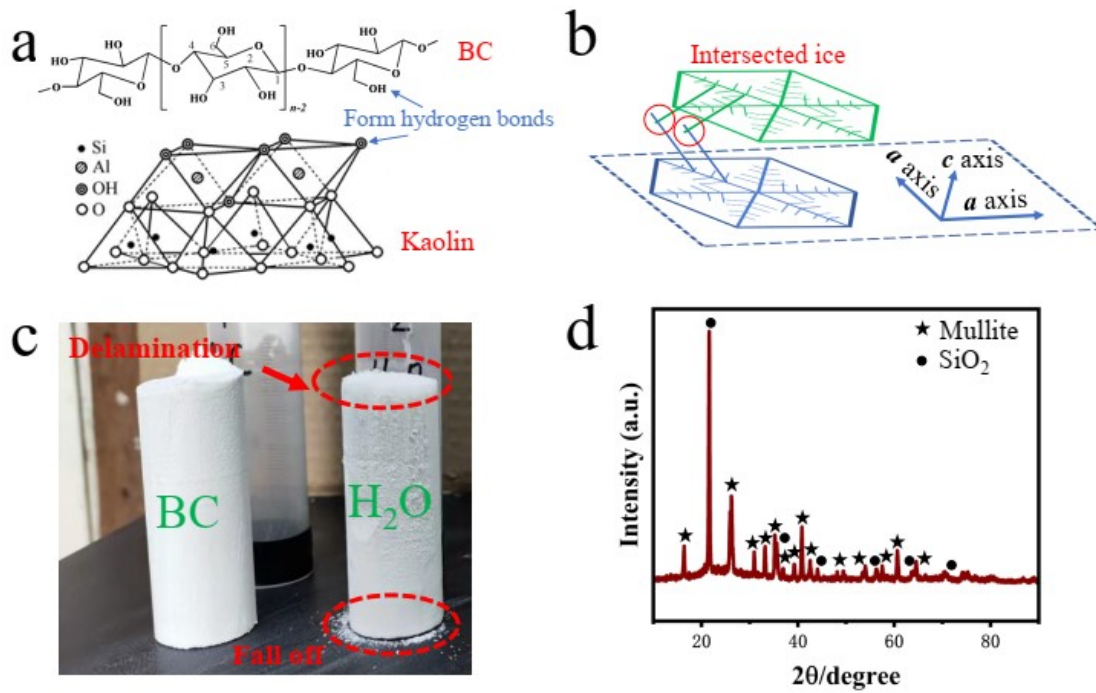
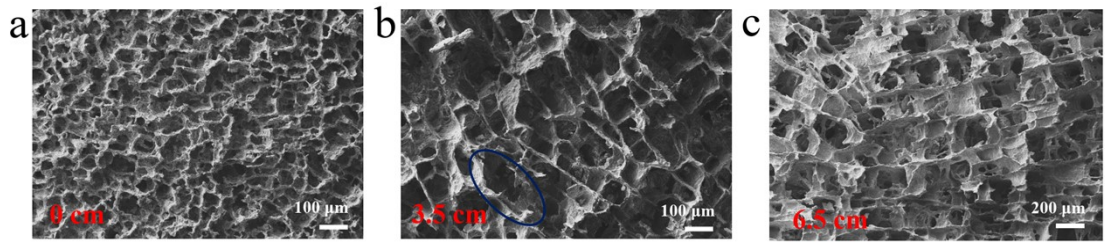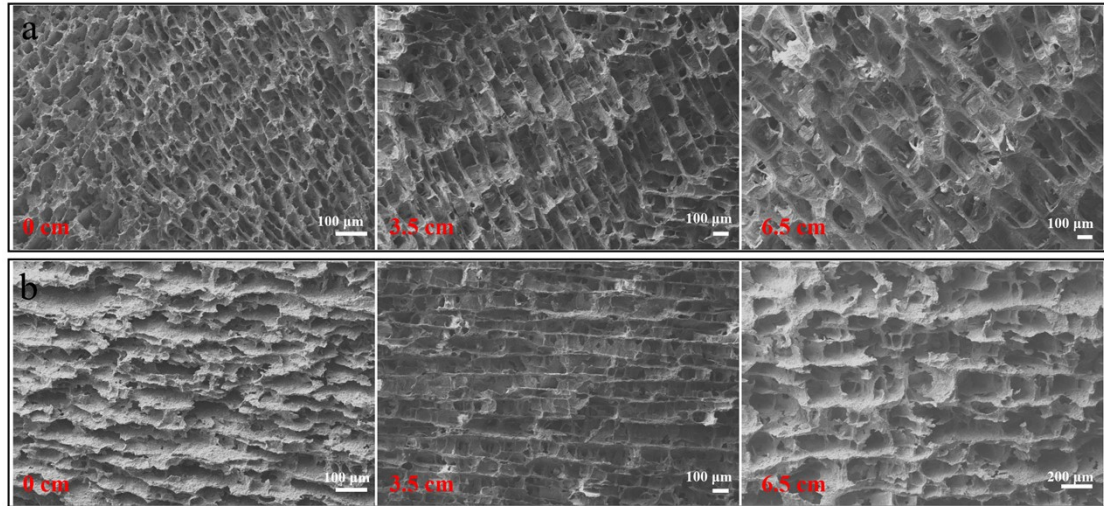**Fig. S4** (a) Structure of Kaolin and BC. (b) The diagram of the growth of ice crystals. (c) Dry billets. (d) XRD pattern of the porous ceramic.

229

230   **Fig. S5** (a-c) SEM picture of the cross-sections at different heights of the ceramic

231   with a solid content of 15 wt% prepared at -45 °C.

232

Fig. S6 SEM picture of the (a) cross-sections and (b) longitudinal section at different heights of the ceramic with a solid content of 20 wt% prepared at -45 °C.
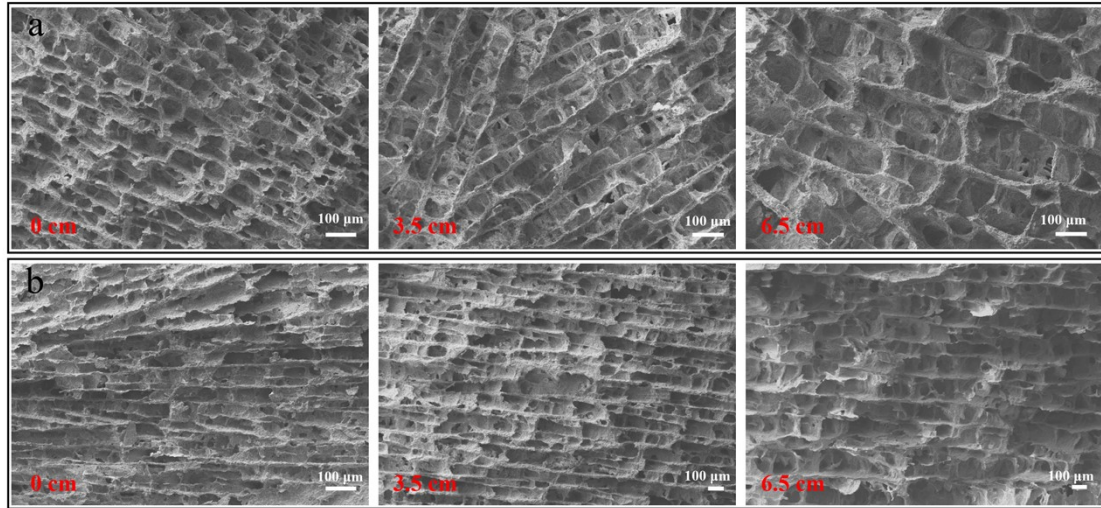
237

238 **Fig. S7** SEM picture of the (a) cross-sections and (b) longitudinal section at different

239   heights of the ceramic with a solid content of 25 wt% prepared at -45 ℃.

240

241 **Table S2** The average open porosity of different porous ceramics

Solid content	15 wt%	20 wt %	25 wt %
Average open porosity	0.805	0.767	0.744

242

243
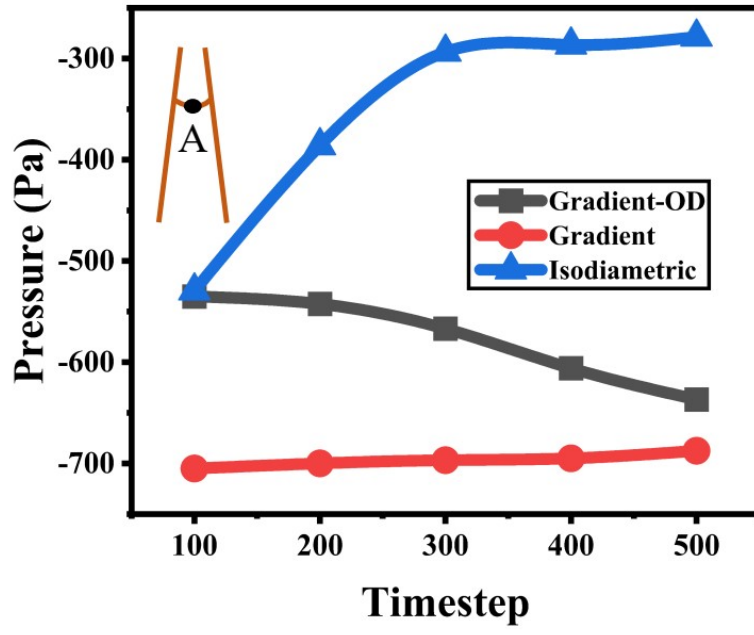
244

245 **Fig. S8** The simulated changes of pressure of point A at the bottom of the meniscus of

246 different capillaries.

247

248
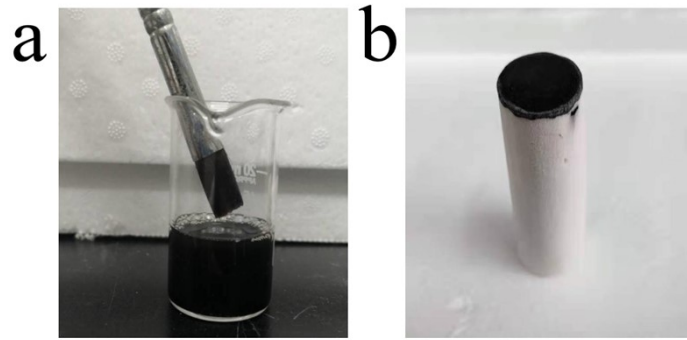
Fig. S9 (a) Digital images of MGO dispersion. (b) Porous ceramics coated with MGO.

250
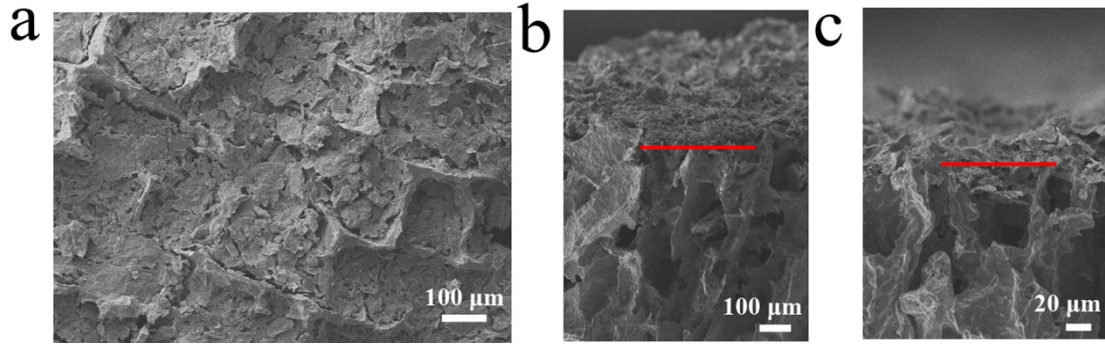
Fig. S10 (a) SEM picture of the cross-section of the MGO covered on the surface of the Gradient porous ceramic. SEM picture of the longitudinal section of the MGO covered on the surface of the: (b) Gradient porous ceramic. (c) Gradient-OD porous ceramic.

257
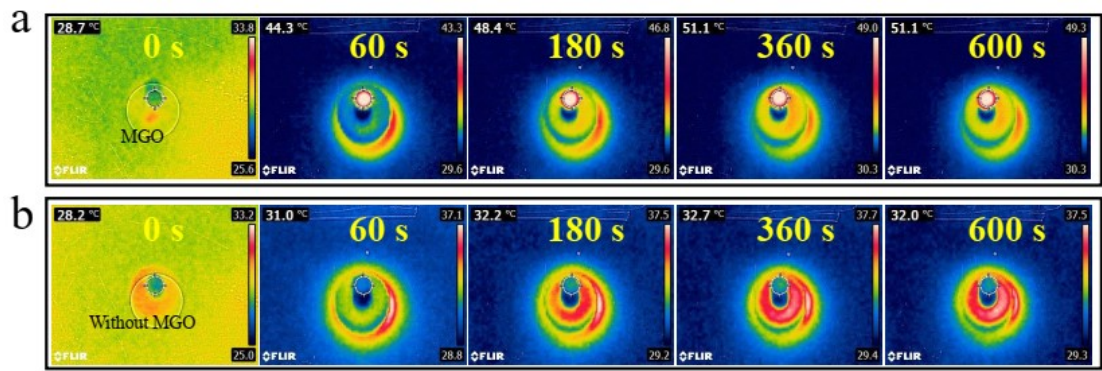
258 **Fig. S11** (a, b) The infrared thermographs of temperature change.

259
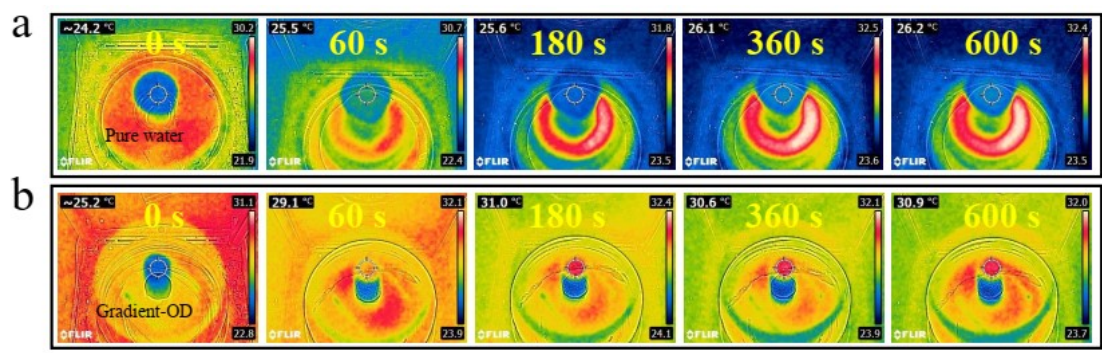
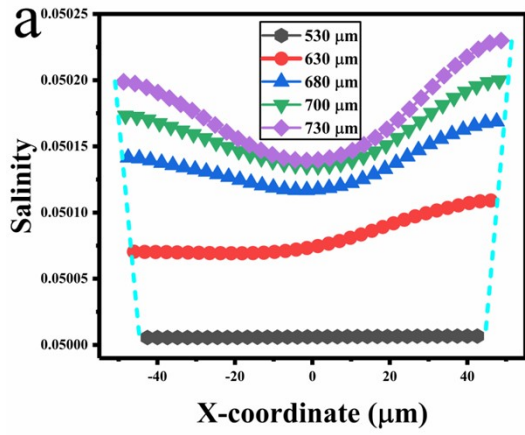**Fig. S12** (a, b) The infrared thermographs of temperature change.

263
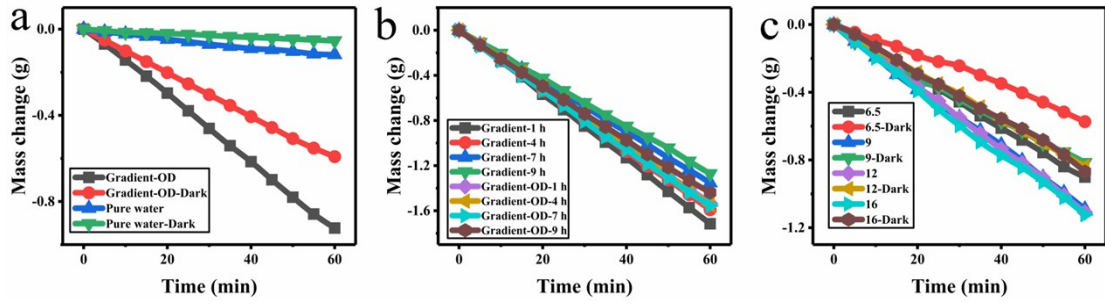
Fig. S13 (a-c) The mass change.

264

265
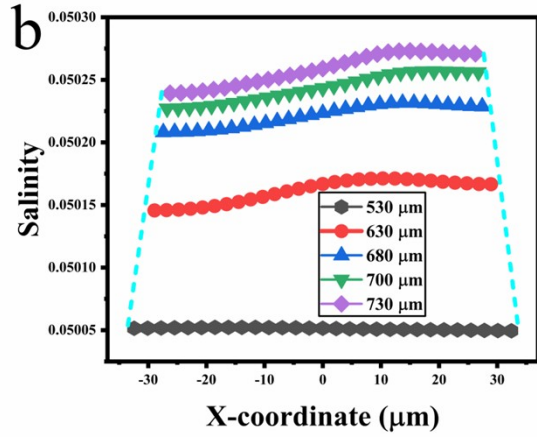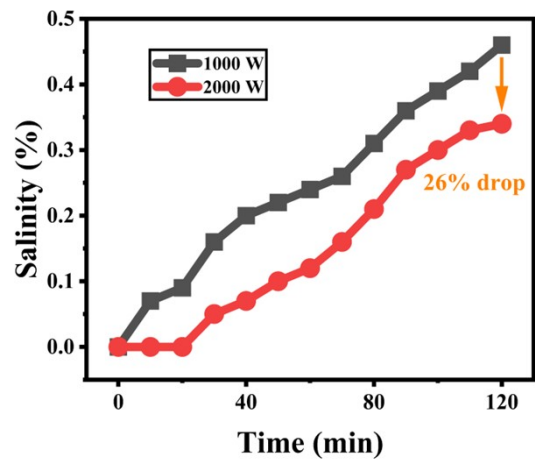
266

267 **Fig. S14** The variation of salinity with the X-coordinate at different heights of (a) Gradient tube
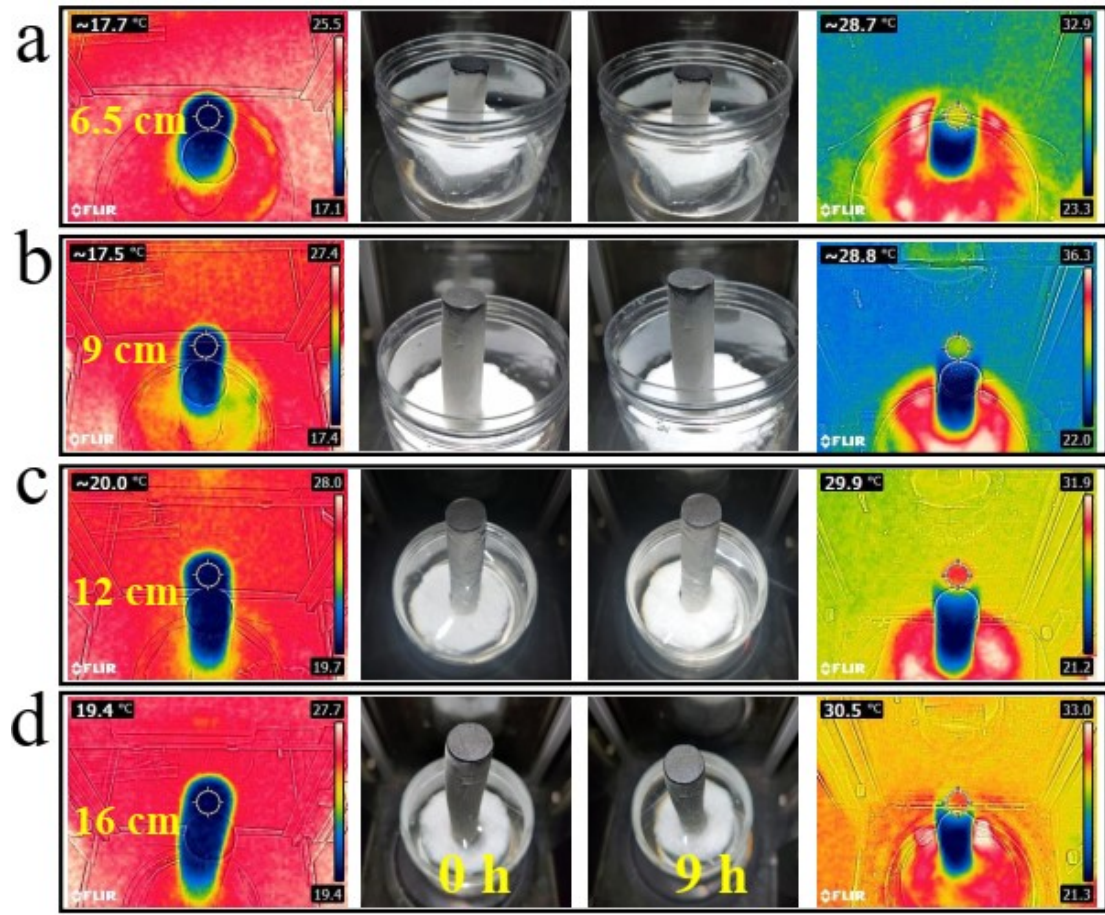
268 and (b) Gradient-OD tube.

269

Fig. S15 The variation of salinity of bulk water under different irradiation with Gradient porous ceramic
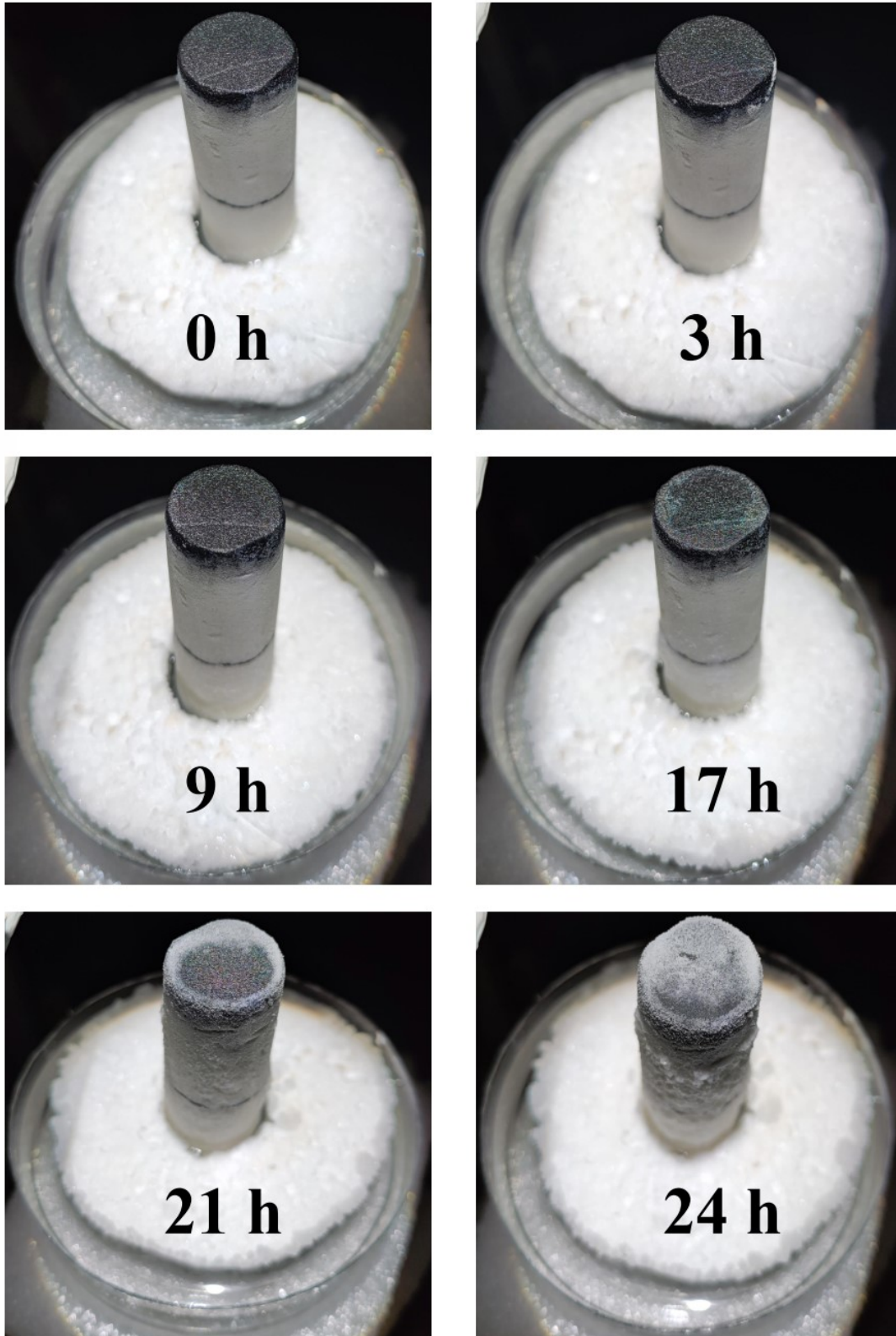
Fig. S16 The infrared thermographs of temperature change and the digital photos of the evaporation surface before and after evaporation.

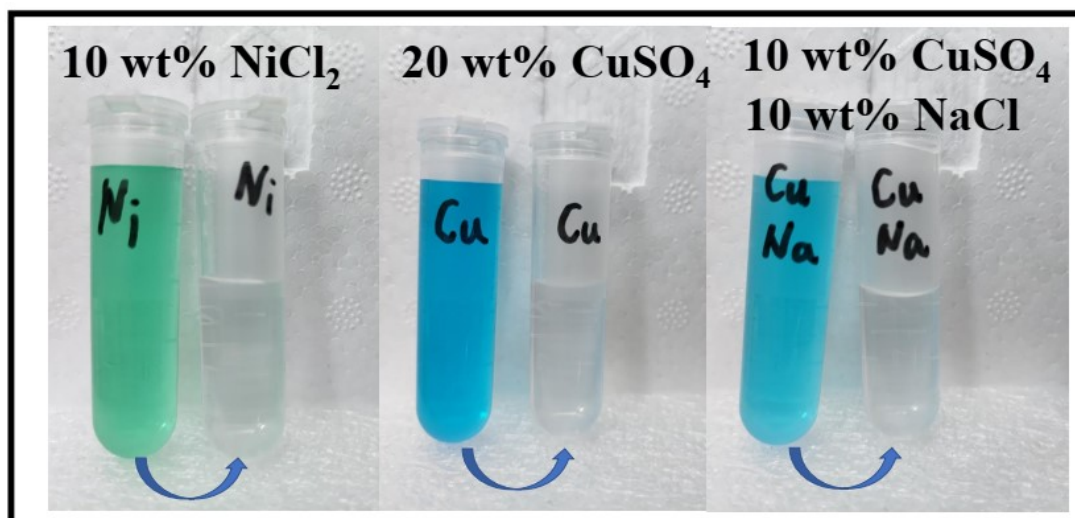**Fig. S17** Image of salt crystal in the surface of the evaporator after different evaporation time.

Fig. S18 Schematic diagram of the solution before and after treatment.

283 **Table S3** Comparing various wood-based or tree-inspired evaporators under 1 sun

284 illumination.

Species	Length of evaporators (cm)	Evaporation rate $(kg \cdot m^{-2} \cdot h^{-1})$	Efficiencies (%)	Brine salinity (wt%)	Ref.
Porous ceramic coated with MGO	**6.5**	**3.28**	**80**	**23**	**This work**
Bilayer wood with surface carbonization	3	about 1	57.3	1.05	5
Carbonized bilayer wood with bimodal porous structure	0.45	0.8	57	15	6
Radially, hierarchically structured aerogels	5	2	85.7	null	7
Chinese ink coating wood with drilling holes	2.5	1.6	74	3.5	8
Wood coated with polydopamine and silver nanoparticles	4.5	1.58	88.6	0.97	9
Wood-derived aerogel coated with Au–rGO	null	1.394	90.1	3	10
Fe_3O_4 coated delignified wood	3	1.3	73	3.5	11

285

286

S4 References

1   C. Hirt, and B. Nichols, *J. Comput. Phys.*, 1981, **39**, 201-225.

2   J. Pilliod and E. Puckett, *J. Comput. Phys.*, 2004, **199**, 465-502.

3   W. Rider and D. Kothe, *J. Comput. Phys.*, 1997, **141**, 112-152.

4   J. Brackbill, D. Kothe and C. Zemach, *J. Comput. Phys.,* 1992, **100**, 335-354.

5   M. Zhu, Y. Li, G. Chen, F. Jiang, Z. Yang, X. Luo, Y. Wang, S. Lacey, J. Dai, C. Wang, C. Jia, J. Wan, Y. Yao, A. Gong, B. Yang, Z. Yu, S. Das and L. Hu, *Adv. Mater.*, **29**, 1704107.

6   S. He, C. Chen, Y. Kuang, R. Mi, Y. Liu, Y. Pei, W. Kong, W. Gan, H. Xie, E. Hitz, C. Jia, X. Chen, A. Gong, J. Liao, J. Li, Z. Ren, B. Yang, D. Siddhartha and L. Hu, *Energy Environ. Sci.*, 2019, **12**, 1558-1567.

7   W. Xu, Y. Xing, J. Liu, H. Wu, Y. Cui, D. Li, D. Guo, C. Li, A. Liu and H. Bai, *ACS Nano*, 2019, **13**, 7930-7938.

8   X. Zhang, Z. Wang, L. Song, Y. Feng and J. Yao, *Desalination*, 2020, **496**, 114727.

9   J. Yang, Y. Chen, X. Jia, Y. Li, S. Wang and H. Song, *ACS Appl. Mater. Interfaces*, 2020, **12**, 47029–47037.

10   Q. Zhang, L. Li, B. Jiang, H. Zhang, N. He, S. Yang, D. Tang and Y. Song, *ACS Appl. Mater. Interfaces*, 2020, **12 (25)**, 28179–28187.

11   L. Song, X. Zhang, Z. Wang, T. Zhang and J. Yao, *Desalination*, 2021, **507**, 115024.